Intense Turquoise and Green Colors in Brownmillerite-Type Oxides Based on Mn^{5+} in Ba$_2$In$_{2-x}$Mn$_x$O$_{5+x}$

Peng Jiang,[†] Jun Li,[†] A. Ozarowski,[‡] Arthur W. Sleight,[†] and M. A. Subramanian*,[†]

[†]Department of Chemistry, Oregon State University, Corvallis, Oregon 97331, United States
[‡]National High Magnetic Field Laboratory, Florida State University, Tallahassee, Florida 32310, United States

S *Supporting Information*

ABSTRACT: Brownmillerite-type oxides Ba$_2$In$_{2-x}$Mn$_x$O$_{5+x}$ ($x = 0.1-0.7$) have been prepared and characterized. Magnetic measurements indicate that manganese in as-prepared samples is substituting predominantly as Mn^{5+} for all values of x with observed paramagnetic spin-only moments close to values expected for two unpaired electrons. Electron paramagnetic resonance measurements indicate that this Mn^{5+} is present in a highly distorted tetrahedral environment. Neutron diffraction structure refinements show that Mn^{5+} occupies tetrahedral sites for orthorhombic ($x = 0.1$) and tetragonal ($x = 0.2$) phases. For Mn ≥ 0.3 samples, neutron refinements show that the phases are cubic with disordered cations and oxygen vacancies. The colors of the phases change from light yellow ($x = 0$) to intense turquoise ($x = 0.1$) to green ($x = 0.2, 0.3$) or to dark green ($x \geq 0.4$). Under reducing conditions, Mn^{5+} is reduced to Mn^{3+}, and Ba$_2$In$_{2-x}$Mn$_x$O$_{5+x}$ phases become black Ba$_2$In$_{2-x}$Mn$_x$O$_5$ phases still with the brownmillerite structure.

1. INTRODUCTION

Our recent discovery[1,2] of oxides with exceptional blue colors based on Mn^{3+} in trigonal-bipyramidal coordination has prompted us to explore manganese in other oxide hosts. Inorganic compounds containing Mn^{5+} in tetrahedral coordination are known to show strong optical absorption, producing turquoise- to green-colored compounds.[3−5] However, Mn^{5+} is generally not stable in oxides. Even MnO$_2$ decomposes in air, losing O$_2$ at about 530 °C. Oxidation states for manganese higher than 4+ tend to be even more unstable but can be stabilized in oxides with basic cations such as Ba^{2+}. We have discovered that manganese substitutes for indium in Ba$_2$In$_2$O$_5$ as Mn^{3+} under our high-temperature synthesis conditions, but this manganese oxidizes to Mn^{5+} upon cooling in air and produces materials with intense turquoise to green colors.

Ba$_2$In$_2$O$_5$ and related compounds have been intensively studied because of their high O^{2-} ionic conductivity, which can potentially be applied in areas such as solid oxide fuel cells and electrolytes.[6] Ba$_2$In$_2$O$_5$ adopts a brownmillerite-type structure, which can be considered to be an oxygen-deficient perovskite structure with alternating layers of indium octahedra and tetrahedra. A version of the brownmillerite structure is shown in Figure 1. The tetrahedra share corners to form continuous chains along the shortest axis. There are, however, two different configurations possible for these chains (Figure 2). Simple ordering of chain configurations typically leads to the structures described in space groups $I2mb$ or $Pnma$. Complex chain ordering can occur, and complete disorder of chain configurations gives space group $Icmm$. According to a brownmillerite structure map,[7] Ba$_2$In$_2$O$_5$ is expected to have disordered chain configurations, thus giving space group $Icmm$. In fact, the most recent structure refinements for Ba$_2$In$_2$O$_5$ do reject space groups $I2mb$ and $Pnma$ in favor of $Icmm$.[8,9] Thus, the two configurations of the tetrahedral chains are considered to be disordered. However, electron microscopy for Ba$_2$In$_2$O$_5$
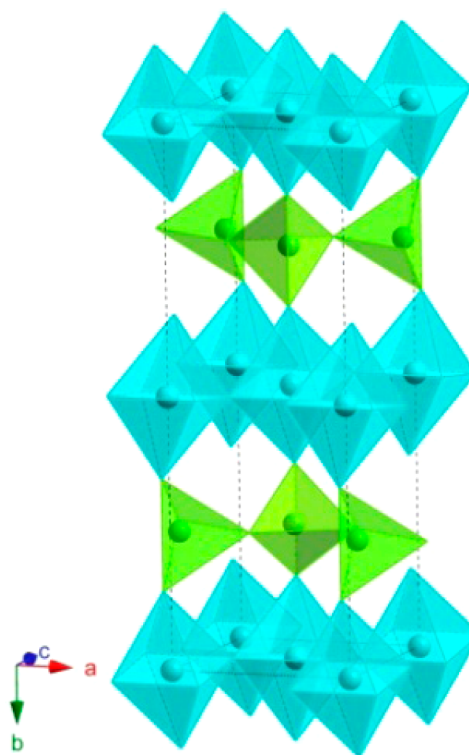

Figure 1. $Pnma$ version of the brownmillerite structure where the two chains shown have different configurations. Octahedra are turquoise, and tetrahedra are green.

shows a very complex superstructure, indicating that the configurations of the chains are ordered.[9] This superstructure is
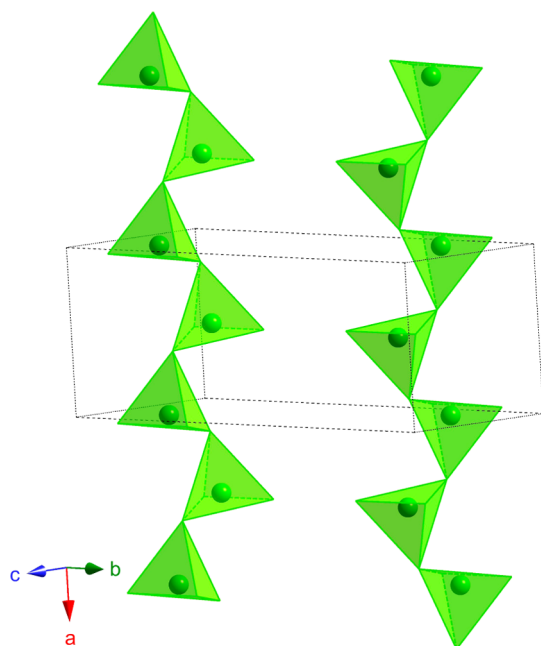
Figure 2. Chains of tetrahedra along the *a* axis in the *Pnma* orthorhombic structure showing the two chain configurations. Only one of these chain configurations is present in the *I2mb* version of the brownmillerite structure. In space group *Icmm*, a disordered mixture of these two configurations is assumed. In all cases, the chains are all oriented along the short axis. Chains are along the *a* axis in space group *Pnma* but along the *c* axis in space group *Icmm*. The strong bonding along the chains results in $c > a$ in space group *Pnma* but in $a > c$ in space group *Icmm*.

ignored in the published refinements. Thus, details of the $Ba_2In_2O_5$ structure with regard to the layers containing the tetrahedra are unknown. At high temperatures, $Ba_2In_2O_5$ adopts the ideal cubic perovksite structure with no long-range order of the oxygen vacancies. A tetragonal structure for $Ba_2In_2O_5$ has been reported to occur as an intermediate between the orthorhombic and cubic structures.[8,10] Substitutions of zirconium for indium can stabilize the cubic structure at room temperature.[8] Kobayashi et al. reported the substitution for indium of all of the first-row transition elements.[11] Such substitutions generally increased the symmetry to tetragonal or cubic. The ionic conductivity was reported for all substitutions, but no information was provided on the color or magnetic properties.

Compounds of the type $A_5(MO_4)_{3-x}(Mn^{5+}O_4)_xX$ with A = Ba, Sr, and Ca, M = P, As, and V, and X = Cl, OH, and F are known to exhibit a turquoise color at low x, changing to green at higher values of x.[3−5] Similar results have been reported for $Ba_3(P_{1-x}Mn_xO_4)_2$ phases.[12] The origin of this color is a valley in the visible absorption at a wavelength of about 450 nm. A commercial pigment with Mn^{5+} doped into $BaSO_4$ has been termed manganese blue; however, production of this pigment has been largely discontinued mostly because of pollution issues associated with its production. A new host is required for the Mn^{5+} chromophor if it is to regain the importance it once had in commercial pigments. Although manganese is well-known in the brownmillerite structure, an oxidation state for manganese as high as 5+ has not been previously reported in this structure.

2. EXPERIMENTAL SECTION

A solid-state method was used for the synthesis of all $Ba_2In_{2-x}Mn_xO_{5+x}$ samples. A stoichiometric mixture of $BaCO_3$ (Baker Analyze, >99%), In_2O_3 (Stanford Materials, >99.99%), and Mn_2O_3 (JMC, >98%) was thoroughly ground in an agate mortar. The powder mixture was then pressed into pellets with an applied pressure of 1 psi. The pellets were heated at 1200 °C for 12 h in air, reground, pelletized again, and finally heated at 1300 °C for another 12 h. Some powder samples were later reduced in a H_2/N_2 gas mixture (5% H_2) at 500 °C for 4 h.

X-ray diffraction (XRD) patterns were obtained at room temperature with a Rigaku Miniflex diffractometer using Cu Kα radiation and a graphite monochromator on the diffracted beam. X-ray data used for cell-edge refinement were collected over a 2θ range of 10−120° using a step size of 0.02 with 2 s of counting at each step.

Room temperature neutron diffraction data for $Ba_2In_{2-x}Mn_xO_{5+x}$ samples were collected at the National Institute of Standards and Technology (NIST) Center for Neutron Research for $x = 0.1$ and 0.5 and the Spallation Neutron Source (SNS) at Oak Ridge National Laboratory (ORNL) for $x = 0.1, 0.2, 0.4,$ and 0.6. Low-temperature neutron data for $x = 0.4$ and 0.6 were collected at 12 K at ORNL.

Time-of-flight (TOF) neutron data were collected using the Powgen powder diffractometer at the SNS at ORNL. Samples of about 3.9 g were contained in vanadium cans of 10 mm in diameter and analyzed over d spacings of 0.6−8.3 Å. Constant-wavelength neutron data were collected using the BT-1 32-detector high-resolution diffractometer at the NIST Center for Neutron Research at the NIST. A Cu(311) monochromator, which has a takeoff angle of 90° and $\lambda = 1.5401(2)$ Å was employed. A collimation of 15′ of the arc was used before the monochromator, 20′ before the sample, and 7′ before the detectors. The samples were loaded into vanadium containers of 15.6 mm in diameter and 50 mm in length. Data were collected at room temperature over a 2θ range of 3−166° with a step size of 0.05°.

Crystal structures were refined by the Rietveld method using the *GSAS* software package with the *EXPGUI* interface.[13,14] TOF peak-profile function no. 3 (tabulated α, β, and ΔT forms) and a shifted Chebyschev function were used for modeling of the diffraction peaks and background, respectively. The small amount of vanadium impurity from the sample holder was fitted as a second phase for TOF data refinements.

Magnetic data were obtained on a Quantum Design Physical Property Measuring System over a temperature range of 5−300 K. Data were collected using the zero-field cooling method with an applied magnetic field of 0.5T. Diamagnetic corrections were applied to the magnetic data.[15]

Diffuse-reflectance spectra utilized a fiber-optic system. Light from a light source was passed through a bifurcated (Y-shaped) optical fiber assembly onto the sample and back into the bifurcated optical fiber, where it was taken to a spectrophotometer. $BaSO_4$ was used as a reference, and the data were transformed into absorbance using the Kubelka−Munk function.[16]

High-field, high-frequency electron paramagnetic resonance (EPR) spectra at temperatures ranging from ca. 6 to 290 K were recorded on a home-built spectrometer at the EMR facility of the NHMFL.[17]

The instrument is a transmission-type device in which microwaves are propagated in cylindrical lightpipes. The microwaves were generated by a phase-locked Virginia Diodes source generating a frequency of 13 ± 1 GHz and producing its harmonics up to the 32nd. A superconducting magnet (Oxford Instruments) capable of reaching a field of 17 T was employed.

3. RESULTS

Single-phase $Ba_2In_{2-x}Mn_xO_{5+x}$ samples were successfully prepared at 1300 °C in air with x up to 0.7 (Figure 3). For samples with a higher manganese content, impurity peaks appeared in the XRD patterns. Both XRD and neutron powder diffraction data were collected to analyze the structure of these phases. The orthorhombic symmetry of $Ba_2In_2O_5$ is maintained
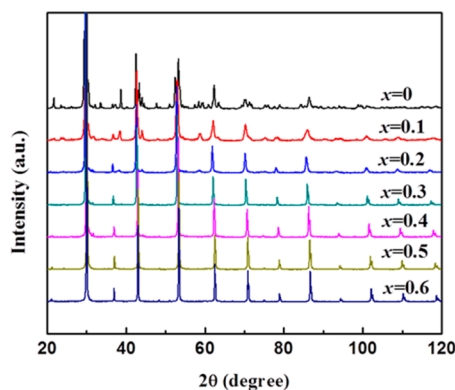
Figure 3. XRD patterns of $Ba_2In_{2-x}Mn_xO_{5+x}$ samples (x = 0−0.6).

for x = 0.1. The symmetry has increased to tetragonal for x = 0.2. Cubic symmetry with a unit cell expected for the ideal perovskite structure is indicated for samples with x = 0.3−0.7. The peaks associated with oxygen vacancy ordering and the two sites for indium (manganese) have disappeared for the cubic patterns. This symmetry evolution is consistent with that reported.[11] The unit-cell edges versus x are given in Figure 4.
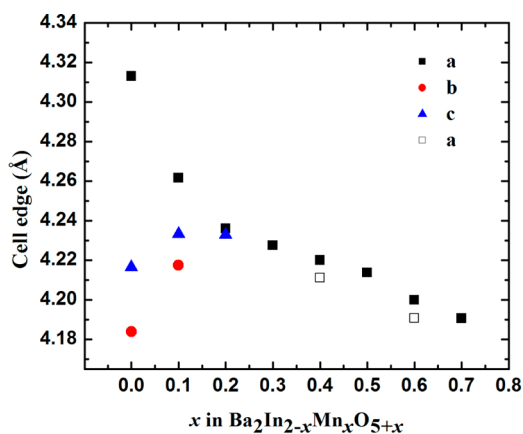

Figure 4. Cell edges for $Ba_2In_{2-x}Mn_xO_{5+x}$ phases as a function of x. For the orthorhombic x = 0.0 and 0.1 phases, a and c are divided by $\sqrt{2}$ and b is divided by 4. For the tetragonal phase with x = 0.2, a and b are divided by $\sqrt{2}$ and c is divided by 4. This allows a direct comparison with the values for the cubic phases. The open squares are unit-cell parameters from low-temperature (12 K) neutron data.

Our structural studies are based on the Rietveld fitting of neutron diffraction patterns. Two independent studies have recently concluded that the most appropriate space group to describe the room temperature structure of $Ba_2In_2O_5$ is $Icmm$[6,7] This space group was found to be suitable for our Rietveld refinements of orthorhombic $Ba_2In_{1.9}Mn_{0.1}O_{5.1}$. The results are summarized in Table 1 and in an available CIF file. The occupancy of the O3 site cannot exceed 0.5 because in this disordered model O3 atoms are in pairs located only 1.6 Å apart. Each such pair can therefore have a maximum of one O atom. The extra O atom would most likely be in a site considered to be the oxygen vacancy site relative to the perovskite structure. Refining the occupancy of oxygen at this ideal site led to the expected value for the composition, and the refined U value was reasonable. Refinement of the manganese content on the In2 site is also in good agreement with the

nominal composition. No evidence was found for manganese on the In1 site.

For $Ba_2In_{1.8}Mn_{0.2}O_{5.2}$, the unit cell has become metrically very close to cubic (Figure 4), but it is actually tetragonal. A tetragonal structure for $Ba_2In_2O_5$ at 962 °C has been reported.[10] The space group used to fit the neutron powder diffraction data obtained at this temperature was $I4/mcm$. Our Rietveld refinements of tetragonal $Ba_2In_{1.8}Mn_{0.2}O_{5.2}$ were also conducted in space group $I4/mcm$. Refinement details are shown in Table 2 and in an available CIF file. Our refinements indicate that manganese resides again almost exclusively in the "tetrahedral layer" and is displaced by about 0.5 Å off the 4-fold axis containing both In atoms. Because of the high degree of disorder in the In2/Mn layer, the precise environment of manganese cannot be established. However, the manganese displacement off the 4-fold axis leads to a Mn−O distance of 1.62 Å, in comparison to the In2−O distance of 2.12 Å. This distance is close to that expected for Mn^{5+}. Separate refinements for In2 and Mn might not seem justified in view of the relative amount of Mn. However, two factors combine to make this possible: (1) the large difference in scattering amplitudes (−3.75 fm for Mn vs +4.065 fm for In) and (2) the large size difference between In^{3+} and Mn^{5+}. Refinement of the In2/Mn ratio in this layer agrees well with the value expected based on the composition, and this supports the validity of refining separate positional parameters for manganese. Because of the disorder present, the precise environment of manganese likely varies somewhat from site to site. Separate refinements for the manganese position failed for orthorhombic $Ba_2In_{1.9}Mn_{0.1}O_{5.1}$ because of the lower amount of manganese. An increase in the oxygen content of the In2/Mn layer increases the average coordination number of indium; thus, the average indium displacement in this layer relative to the ideal perovskite site is smaller than that for phases with x = 0.0 and 0.1. This displacement can now be accounted for simply on the basis of an anisotropic displacement factor.

The size and shape of the ellipsoids in tetragonal $Ba_2In_{1.8}Mn_{0.2}O_{5.2}$ indicate the range of positional parameters caused by the disorder (Figure 5). The ellipsoid for In2 atoms indicates strong displacements perpendicular to the c axis; however, Mn atoms (shown for only one site) are displaced much more, as would be expected for mangnaese to achieve a tetrahedral environment. The displacements of manganese off the 4-fold axis are in the direction expected. The O3 site is 61% occupied, and its ellipsoid shape is consistent with various positions for this oxygen in forming a tetrahedral environment around manganese and some In2 as well as forming an octahedral environment around some In2. The ellipsoids for Ba and O2 are close to normal but somewhat large because of the disorder. The ellipsoid shapes for In1 and O1 indicate disordered static displacements along the c axis. This reflects a buckling of the octahedral layer. Such a buckling also occurs for orthorhombic $Ba_2In_{1.9}Mn_{0.1}O_{5.1}$, leading to In1−O1−In1 angles of 175° instead of the ideal 180°. For tetragonal $Ba_2In_{1.8}Mn_{0.2}O_{5.2}$, the space group of $I4/mcm$ constrains the In−O−In angles to 180°, but the displacement factors indicate that the buckling is still present but is not completely ordered. When we have well-formed chains of tetrahedra in this structure, they occur along either the a or b axis. The cell edge along which chains form shrinks because of the stronger bonding along the chains, causing a reduction in the symmetry from tetragonal to orthorhombic. The tetragonal symmetry we observe for $Ba_2In_{1.8}Mn_{0.2}O_{5.2}$ thus indicates that the chains are

Table 1. TOF Neutron Structural Refinement of Orthorhombic $Ba_2In_{1.9}Mn_{0.1}O_{5.1}$.

General Information	
space group	$Icmm$
a (Å)	6.0280(2)
b (Å)	16.873(1)
c (Å)	5.9832(2)
V (Å³)	608.55(3)
R_p (%)	2.81
wR_p (%)	1.66

Wyckoff Positions, Atomic Coordinates, and Occupancy						
Wyckoff	site	x	y	z	occupancy	U_{iso} (Å²)
8h	Ba	0.5011(3)	0.6117(2)	0	1.00	0.0061
4a	In1	0	0	0	1.00	0.0081
8i	In2	0.541(1)	$^1/_4$	0.464(1)	0.45(1)	0.008(2)
8i	Mn2	0.541(1)	$^1/_4$	0.464(1)	0.05(1)	0.008(2)
8g	O1	$^1/_4$	0.9948(2)	$^1/_4$	1.00	0.0066
8h	O2	0.0166(4)	0.1349(2)	0	1.00	0.0408
8i	O3	0.656(1)	$^1/_4$	0.158(1)	0.50	0.0306
4c	O4	$^1/_4$	$^1/_4$	$^1/_4$	0.11(1)	0.039(3)

Anisotropic Thermal Displacement Parameters						
	U_{11} (Å²)	U_{22} (Å²)	U_{33} (Å²)	U_{12} (Å²)	U_{13} (Å²)	U_{23} (Å²)
Ba	0.0057(2)	0.0105(2)	0.0042(2)	0.0073(3)	0	0
In1	0.0043(3)	0.0165(3)	0.0040(3)	0.0040(3)	0	0
O1	0.0052(2)	0.0091(2)	0.0054(2)	0	−0.0016(2)	0
O2	0.0540(1)	0.0328(1)	0.0356(1)	0.0010(1)	0	0
O3	0.038(3)	0.019(2)	0.034(3)	0	0.026(2)	0

Table 2. TOF Neutron Structural Refinement of Tetragonal $Ba_2In_{1.8}Mn_{0.2}O_{5.2}$

General Information	
space group	$I4/mcm$
a (Å)	5.9896(4)
b (Å)	5.9896(4)
c (Å)	16.949(2)
V (Å³)	608.05(2)
R_p (%)	2.65
wR_p (%)	1.60

Wyckoff Positions, Atomic Coordinates, and Occupancy						
Wyckoff	site	x	y	z	occupancy	U_{iso} (Å²)
8g	Ba	0	$^1/_2$	0.6310(5)	1.00	0.0226
4c	In2	0	0	0	0.76(1)	0.0379
4a	In1	0	0	$^1/_4$	1.00	0.0207
16k	Mn2	0.087(3)	0.969(3)	0	0.06(1)	0.005(2)
8e	O1	$^1/_4$	$^1/_4$	$^1/_4$	1.00	0.0395
8h	O3	0.735(3)	0.235(3)	0	0.61(1)	0.0989
8f	O2	0	0	0.121(3)	1.00	0.0427

Anisotropic Thermal Displacement Parameters						
	U_{11} (Å²)	U_{22} (Å²)	U_{33} (Å²)	U_{12} (Å²)	U_{13} (Å²)	U_{23} (Å²)
Ba	0.018(2)	0.018(2)	0.032(4)	0.004(3)	0	0
In2	0.050(3)	0.050(3)	0.014(4)	0	0	0
In1	0.004(1)	0.004(1)	0.054(4)	0	0	0
O1	0.015(2)	0.015(2)	0.098(4)	−0.013(2)	0.016(4)	−0.016(4)
O3	0.126(6)	0.126(6)	0.020(4)	0.120(6)	0	0
O2	0.051(2)	0.051(2)	0.026(3)	0	0	0

no longer extended along just one direction. The chains have been disrupted by manganese substitution and the extra oxygen. Chain fragments may remain with an equal probability of occurring along the a or b axis. A comparison of the In−O distances for $Ba_2In_2O_5$, $Ba_2In_{1.9}Mn_{0.1}O_{5.1}$, and $Ba_2In_{1.8}Mn_{0.2}O_{5.2}$ is given in Table 3. The In1−O distances should be quite

reliable, but the In2−O distances are less so because of the disorder.

All of the stronger superstructure peaks for tetragonal $Ba_2In_{1.8}Mn_{0.2}O_{5.2}$ could be indexed with a unit cell with $Z = 2$, $a = 4.235$ Å, and $c = 8.487$ Å. Such a unit cell has been suggested
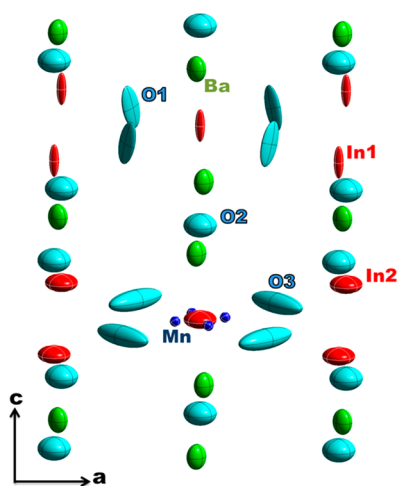
Figure 5. Ellipsoids for tetragonal $Ba_2In_{1.8}Mn_{0.2}O_{5.2}$. Color code: green, Ba; red, In; blue, Mn; turquoise, O. The vertical 4-fold axes go through both In1 and In2.

Table 3. Comparison of Distances for the $Ba_2In_{2-x}Mn_xO_{5+x}$ Phases[a]

	$Ba_2In_2O_5$[8]	$Ba_2In_{1.9}Mn_{0.1}O_{5.1}$	$Ba_2In_{1.8}Mn_{0.2}O_{5.2}$
a	6.099	6.028	5.990
b	16.73	16.87	5.990
c	5.962	5.983	16.95
In1−O1 (×4)	2.136	2.125	2.118
In1−O2 (×2)	2.315	2.278	2.186
In2−O2 (×2)	2.018	1.985	2.051
In2−O3	2.065	1.967	2.121
In2−O3	2.117	2.164	2.121

[a]All standard deviations are ±3 or smaller for the last digit.

for the structure of $Ba_2In_2O_5 \cdot H_2O$.[18] However, our refinements using this unit cell for $Ba_2In_{1.8}Mn_{0.2}O_{5.2}$ were not stable.

Rietveld refinements for cubic $Ba_2In_{2-x}Mn_xO_{5+x}$ phases with $x = 0.4$, 0.5, and 0.6 were conducted in the $Pm\bar{3}m$ space group for the ideal perovskite structure with just one In/Mn site. The superstructure peaks present in patterns with $x = 0.0$, 0.1, and 0.2 are now absent. The cubic cell edges decrease with increasing manganese substitution (Figure 4) because manganese is smaller than indium regardless of the manganese oxidation state. Details of the Rietveld refinements are listed in Table 4 and in an available CIF file.

For the $x = 0.1$ and 0.2 samples, the refined occupancies of manganese and oxygen are consistent with the $Ba_2In_{2-x}Mn_xO_{5+x}$ formula considering the standard deviations

Table 4. TOF Neutron Structural Refinement of Cubic $Ba_2In_{1-x}Mn_xO_{5+x}$ Samples[a]

Mn x	Mn occupancy	cell a (Å)	wR_p (%)	R_p (%)
0.40	0.36(1)	4.2208(1)	1.60	2.80
0.50	0.46(1)	4.2136(1)	5.73	4.89
0.60	0.56(1)	4.1998(1)	2.41	3.99
Mn x	Ba U_{iso} (Å^2)	In/Mn U_{iso} (Å^2)	O U_{11} (Å^2)	O U_{22} (Å^2)
0.40	0.0211(3)	0.0068(4)	0.0189(6)	0.0427(4)
0.50	0.0188(4)	0.0024(8)	0.0281(9)	0.0404(6)
0.60	0.0241(4)	0.0034(7)	0.028(1)	0.0404(6)

[a]For oxygen anisotropic ADPs, $U_{22} = U_{33}$ and $U_{12} = U_{13} = U_{23} = 0$.

(Tables 1 and 2). Refinement of the NIST data for $Ba_2In_{1.9}Mn_{0.1}O_{5.1}$ gave results similar to those obtained with the ORNL data. However, the agreement factors and standard deviations were not as good as those for the ORNL data. The refined manganese occupancies for the cubic phases ($x = 0.4$, 0.5, and 0.6) increase with increasing x as expected (Table 4). However, the refined x values are always somewhat less than expected. This is likely because of local relaxation at the manganese sites because of the much smaller size of manganese relative to indium. Observed and calculated profiles (room temperature data) are shown in Figures 6−8.
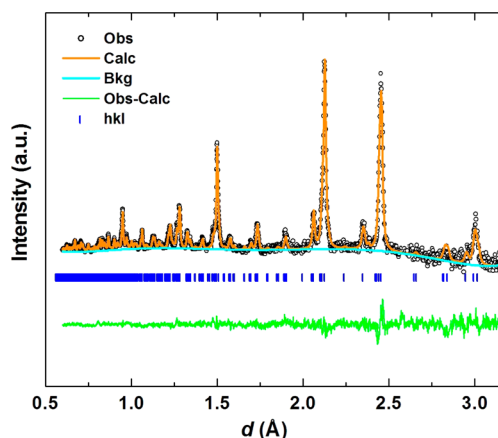

Figure 6. TOF neutron data of orthorhombic $Ba_2In_{1.9}Mn_{0.1}O_{5.1}$ shown with a Rietveld fit. The observed pattern displayed is from the highest-resolution bank (bank 2) with a d-spacing range of 0.60−3.2 Å.
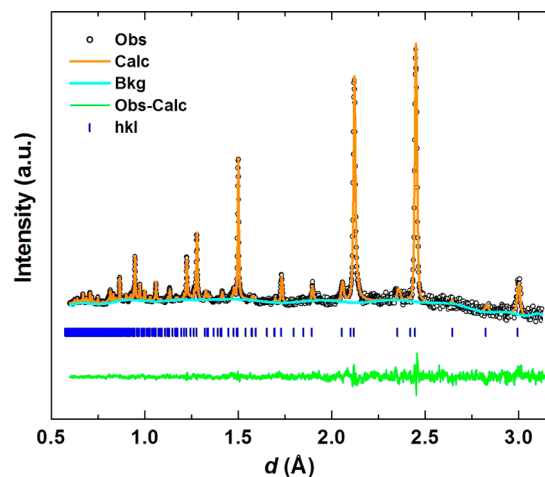

Figure 7. TOF neutron data of tetragonal $Ba_2In_{1.8}Mn_{0.2}O_{5.2}$ shown with a Rietveld fit. The observed pattern displayed is from the highest-resolution bank (bank 2) with a d-spacing range of 0.60−3.2 Å.

A summary of the magnetic measurements is given in Table 5, and plots are presented in Figure 9. The Curie and Weiss constants were derived from the slope and intercept of the straight line region of $1/\chi$ versus T. In the case of $Ba_2In_{2-x}Mn_xO_{5+x}$ samples, the Weiss constant was not significantly different from zero. Thus, the data in Table 5 for these samples is fit to the simple Curie law. Our magnetic susceptibility data for all samples as prepared indicate two unpaired electrons per manganese or slightly more than two unpaired electrons per manganese. This is consistent only with an oxidation state of 5+ for manganese or Mn^{5+} with a small
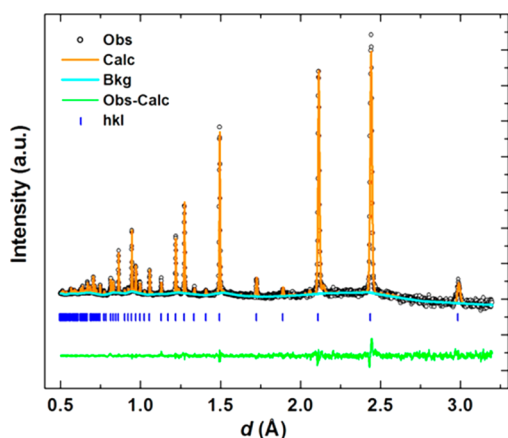
Figure 8. TOF neutron data of cubic $Ba_2In_{1.6}Mn_{0.4}O_{5.4}$ shown with a Rietveld fit. The observed pattern displayed is from the highest-resolution bank (bank 2) with a d-spacing range of 0.60−3.2 Å.

Table 5. Summary of Magnetic Data for $Ba_2In_{2−x}Mn_xO_{5+y}$ Samples As-Prepared and after Reduction*

| | as-prepared $(Ba_2In_{2−x}Mn^{5+}{}_xO_{5+x})$ | | after reduction $(Ba_2In_{2−x}Mn^{3+}{}_xO_{5+y})$ | | |
x	μ (μB)	C/x	μ (μB)	C/x	θ (K)
0.2	2.81	0.20	4.99	0.62	−9.6
0.3	2.79	0.29	4.94	0.90	−13.4
0.4	2.83	0.40			
0.5	2.93	0.53	5.11	1.62	−17.2
0.6	3.07	0.71			
0.7	2.94	0.75			

*Expected spin-only moments (μ_B): 5.92 (Mn^{2+}), 4.90 (high-spin Mn^{3+}), 3.87 (Mn^{4+}), 2.83 (Mn^{5+}), and 1.73 (Mn^{6+}). The Curie constant C is obtained from the Curie−Weiss law: $\chi_m = C/(T + \theta)$ (χ_m is the magnetic susceptibility; θ is the Weiss constant), and the magnetic moment μ was calculated using

$$\mu = \sqrt{\frac{3kC}{N_A}} = 2.84\sqrt{C}\ \mu_B$$

where N_A is Avogardo's number, k is Boltzmann's constant, C is the Curie constant, and μ_B is the Bohr magneton. Because θ was not significantly different from zero for $Ba_2In_{2−x}Mn_xO_{5+x}$ samples, the simple Curie law was used.
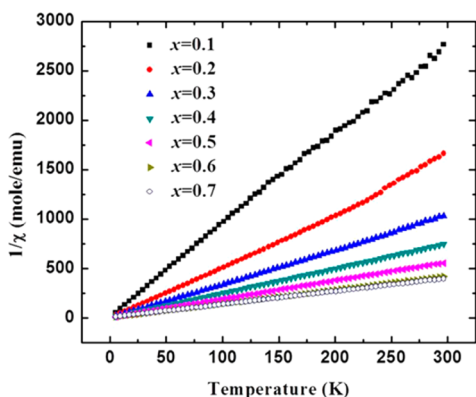

Figure 9. Inverse magnetic susceptibility of $Ba_2In_{2−x}Mn_xO_{5+x}$ for x = 0.1−0.7.

amount of Mn^{4+}. Although low-spin Mn^{3+} would produce the same moment, this species is apparently unknown in oxides.

The oxidation state of manganese in any possible manganese-containing impurity phase would be lower than 5+ and would therefore increase the susceptibility to values higher than we observe. Although as-prepared samples adhere well to the $Ba_2In_{2−x}Mn_xO_{5+x}$ formula, the oxygen content is variable for these samples. For example, heating cubic $Ba_2In_{1.5}Mn_{0.5}O_{5.5}$ under N_2 to 1000 °C resulted in a weight loss of 1.7% and a decrease in the unit-cell edge from 4.211 to 4.192 Å. After samples with x = 0.2, 0.3, and 0.5 are heated under N_2/H_2 at 500 °C, the samples become black and the magnetic moments increase to the extent that the manganese oxidation state is apparently reduced to 3+ (Table 5). Thus, a more general formula for the phases that we have investigated would be $Ba_2In_{2−x}Mn_xO_{5+y}$, where y can be as high as x for samples with Mn^{5+} and as low as 0.0 in phases containing Mn^{3+}. We have not conducted a complete study of the oxygen content for $Ba_2In_{2−x}Mn_xO_{5+y}$ phases under various conditions, but it is clear that the value of y is always less than that of x at the 1300 °C synthesis temperature, with y increasing as the samples are cooled.

The EPR spectra were relatively difficult to obtain, showing line broadening due to metal−metal interactions at higher manganese concentrations, while the diluted samples were prone to microwave saturation effects. Poorly defined, washed-out spectra indicate a nonuniform environment of Mn^{5+} ions. The best spectra were obtained for the $Ba_2In_{1.98}Mn_{0.02}O_{5.02}$ sample at 10 K. The spectrum recorded with a microwave frequency 328.8 GHz is shown in Figure 10. The prominent "forbidden" signal appearing at 5.86 T in Figure 10 was also observed at appropriate magnetic fields at other microwave frequencies and was seen also in other samples with manganese concentrations from 0.01 to 0.3. The resonances at 5.4 and 9.6 T are due to frozen oxygen.[19] The primary spectra could be interpreted using the spin Hamiltonian

$$\hat{H}_S = \mu_B\mathbf{B}\cdot\{\mathbf{g}\}\cdot\hat{S} + D\{\hat{S}_z^2 − S(S + 1)/3\} + E(\hat{S}_x^2 − \hat{S}_y^2)$$

assuming that they were due to the spin state S = 1. The spin Hamiltonian parameters were g_x = 1.973, g_y = 1.965, g_z = 1.968, D = 1.608 cm^{-1}, and E = 0.495 cm^{-1}. The g values are consistent with a less than half-filled d subshell. The **g** tensor is almost isotropic, as expected, and $g_{average}$ of ~1.97 is in good agreement with the literature data for Mn^{5+} in a tetrahedral oxo environment.[5] Large D and E parameters render standard X- or Q-band EPR inapplicable to this problem. Because E is close to $D/3$, the sign of D cannot be determined and is actually irrelevant. The main role of EPR in this work is to confirm the oxidation state on manganese. It is thus noteworthy that no simulation is possible assuming spin states other than S = 1 (see Figure 10). The intense "half-filled" (forbidden) transition at 5.86 T cannot be simulated with the assumption of S = $^3/_2$ (Mn^{4+}) or 2 (Mn^{3+}). The conclusion that manganese is present as Mn^{5+} is thus unambiguous. The large D and E parameters indicate a significant distortion from ideal tetrahedral symmetry, in agreement with our crystallographic and optical data. Large D values ($D > 1$ cm^{-1}) are indeed expected for sufficiently large distortions of the T_d symmetry, as calculated by Reinen et al.[5] In our case, the distortion must destroy the C_3 axis, as judged by the large E parameter, and the distortions must be larger than those in ref 5.

Thermogravimetric analysis (TGA) measurements were conducted in air for both reduced $Ba_2In_{2−x}Mn_xO_5$ and oxidized $Ba_2In_{2−x}Mn_xO_{5+x}$ samples. The weight gain at low temperatures

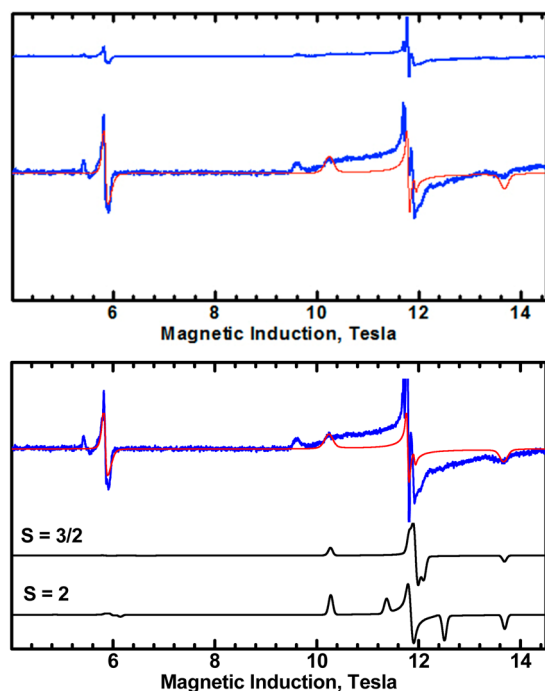**Figure 10.** Blue: High-field EPR spectrum for $Ba_2In_{1.98}Mn_{0.02}O_{5.02}$ recorded at 10 K and 328.8 GHz. The central line at 11.8 T ($g = 2$) is cut off to better show the important features of the spectrum. Red: simulated with $S = 1$, $g_x = 1.973$, $g_y = 1.965$, $g_z = 1.968$, $D = 1.608$ cm^{-1}, and $E = 0.495$ cm^{-1}. Bottom black traces were simulated assuming $S = {}^3/_2$ and 2, with $D = 0.804$, $E = 0.2475$ cm^{-1} and $D = 0.536$, $E = 0.165$ cm^{-1}, respectively, and the same g values as those above. This parameter choice ensures that the outermost "allowed" transitions are calculated at 10.2 and 13.6 T in each case. It is seen that only $S = 1$ produces an intense "half-filled" line at 5.8 T. The resonances at 5.4 and 9.6 T are due to frozen oxygen.

for $Ba_2In_{2-x}Mn_xO_5$ samples and the weight losses at high temperatures for $Ba_2In_{2-x}Mn_xO_{5+x}$ samples were generally consistent with the formulas given. An example is shown in the Supporting Information. However, because of the small amount of weight gain and loss, these results do not exclude the possibility of a small amount of mixed valency in the nominal $Ba_2In_{2-x}Mn_xO_5$ and $Ba_2In_{2-x}Mn_xO_{5+x}$ compositions.

The colors and diffuse-reflectance spectra of the as-prepared $Ba_2In_{2-x}Mn_xO_{5+x}$ phases are shown in Figures 11 and 12. The light-yellow color of the pure $Ba_2In_2O_5$ phase is due to tailing of a band edge into the visible region. Because manganese is substituted for indium, a turquoise to green color develops. The color originates from additional optical absorption at both the high- and low-energy regions of the visible spectrum. The high-energy peak is mainly due to an In–O charge-transfer transition. However, there is now a contribution from Mn–O charge transfer that results in a low-energy shoulder, which then impacts the observed color. The low-energy peak is due to the

allowed transition of a manganese electron from the $^3A_2$ term (resulting from the e^2 configuration) to the $^3T_2$ and $^3T_1$ terms (from the $e^1t_2^1$ configuration). These terms are split by the symmetry being lower than T_d, thus complicating the assignment. Other d–d transitions that give peaks in the visible region are forbidden and thus have very low intensities. The sharp band at 18300 cm^{-1} may be due to the transition $^3A_2 \rightarrow {}^1_aB_2$ (which results from the splitting of the tetrahedral $^1_aT_2$ term.[5] As x increases, the absorption minimum in the middle of the visible region is increasingly filled in, and samples with x higher than 0.3 become darker and finally appear black for $x = 0.7$, even though the minimum in the visible spectrum persists.

4. DISCUSSION

Precise structures for the $Ba_2In_{2-x}Mn_xO_{5+x}$ phases cannot be determined from our neutron diffraction data because of the disorder present. For orthorhombic $Ba_2In_{1.9}Mn_{0.2}O_{5.1}$ and tetragonal $Ba_2In_{1.8}Mn_{0.2}O_{5.2}$, there is no significant disorder with respect to the InO_6 octahedral layer or the Ba position. For the $Ba_2In_{2-x}Mn_xO_{5+x}$ cubic phases ($x = 0.3-0.7$), diffraction patterns present no evidence for the ordering of oxygen vacancies. Substituting a small Mn^{5+} cation (Shannon ionic radius = 0.33 Å) for a large In^{3+} cation (Shannon ionic radius = 0.62 Å) in the tetrahedral layers will necessarily result in significant lattice relaxation around Mn^{5+}. Because of its small size, Mn^{5+} is only known in tetrahedral coordination in oxides. Thus, the fact that we find no evidence for manganese in the octahedral InO_6 layers of orthorhombic $Ba_2In_{1.9}Mn_{0.1}O_{5.1}$ and tetragonal $Ba_2In_{1.8}Mn_{0.2}O_{5.2}$ seems reasonable. At our synthesis temperature of 1300 °C, the situation is very different. $Ba_2In_2O_5$ is cubic above 1040 °C, and the oxygen vacancies are not ordered.[9] The temperature of this transition to cubic for $Ba_2In_{2-x}Mn_xO_{5+y}$ phases decreases with increasing x and has reached room temperature for $x = 0.3$. For phases with $x = 0.1$ and 0.2, oxygen uptake and ordering occur with decreasing temperature. As this occurs, manganese exhibits its preference for the tetrahedral layer.

On the basis of charge-neutrality considerations, the interstitial oxygen introduced with Mn^{5+} substitution would be expected to be attracted to the higher-valent cation Mn^{5+}. However, this would tend to raise the coordination number of Mn^{5+} above 4, which seems unlikely. Size considerations would likely dominate, with the interstitial oxygen raising the coordination of In^{3+} above 4.

The detailed structures of orthorhombic and tetragonal $Ba_2In_2O_5$ are unknown because of the complexity of the ordering of the tetrahedral chains. The situation on substitutions into $Ba_2In_2O_5$ produces an even more complex situation because of the disorder that is introduced. On the basis of previous electron microscopy studies of brownmillerite phases, we might expect that we could have orthorhombic domains despite the lattice that is metrically tetragonal.[20] Electron microscopy might also show regions of order in a
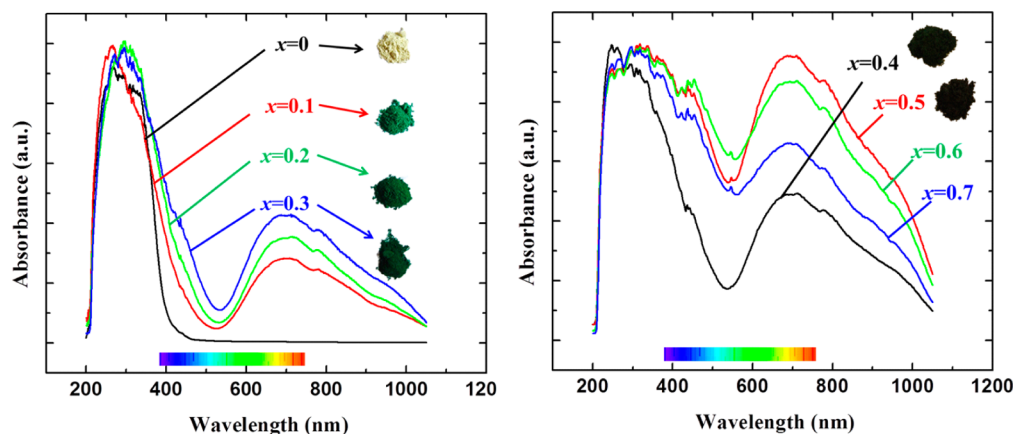

Figure 11. Colors of the $Ba_2In_{2-x}Mn_xO_{5+x}$ samples. Left to right, $x = 0$, 0.1, 0.2, and 0.3.

Figure 12. Diffuse-reflectance spectra for the $Ba_2In_{2-x}Mn_xO_{5+x}$ samples. The spectrum for $x = 0$ ($Ba_2In_2O_5$: white color) is shown for comparison.

disordered matrix, as in the case of $Sr_2Fe_2O_5$.[21] Electron microscopy could elucidate this situation for $Ba_2In_{2-x}Mn_xO_{5+y}$ phases, but this would not likely bring us any closer to a detailed structure, for example, concerning the precise environment of Mn^{5+}. Peak-width analyses for our samples indicate that average crystallite sizes are about 1000 Å or larger. The superstructure peaks were not noticeably broader than the primary peaks; thus, this presents no evidence for domains smaller than crystallites.

Our magnetic susceptibility studies indicate Mn^{5+} for $Ba_2In_{2-x}Mn_xO_{5+x}$ phases and Mn^{3+} for $Ba_2In_{2-x}Mn_xO_5$ phases. Given the dilution of manganese, these conclusions should be reliable. These conclusions are supported by our TGA results. Our optical and EPR results provide unambiguous proof for Mn^{5+} in selected samples. Our optical, EPR, and structural results all indicate a significant distortion from ideal tetrahedral symmetry for Mn^{5+}. A small level of mixed valency for manganese in both as-prepared and reduced samples is likely. At our 1300 °C calcination temperature, the oxidation state of manganese is close to 3+, and oxidation of our samples during cooling is facilitated by the established high O^{2-} mobility in these phases.

ASSOCIATED CONTENT

ⓢ Supporting Information

Neutron crystallographic data in CIF format for $Ba_2In_{2-x}Mn_xO_{5+x}$ (x = 0.1, 0.2, and 0.4) phases and TGA. This material is available free of charge via the Internet at http://pubs.acs.org.

AUTHOR INFORMATION

Corresponding Author

*E-mail: mas.subramanian@oregonstate.edu.

Notes

The authors declare no competing financial interest.

ACKNOWLEDGMENTS

REFERENCES

(1) Smith, A. E.; Mizouguchi, H.; Dlaney, K.; Spaldin, N. A.; Sleight, A. W.; Subramanian, M. A. *J. Am. Chem. Soc.* **2009**, *131*, 17086.
(2) Mizoguchi, H.; Sleight, A. W.; Subramanian, M. A. *Inorg. Chem.* **2011**, *50*, 10.
(3) Grisafe, D. A.; Hummel, F. A. *J. Solid State Chem.* **1970**, *2*, 167−175.
(4) Reinen, D.; Brunold, T. C.; Guedel, H. U.; Yordanov, N. D. *Z. Anorg. Allg. Chem.* **1994**, *624*, 438−442. Reinen, D.; Lachwa, H.; Allmann, R. *Z. Anorg. Allg. Chem.* **1986**, *542*, 71−88.
(5) Reinen, D.; Rauw, W.; Kesper, U.; Atanasov, M.; Güdel, H. U.; Hazenkamp, M.; Oetliker, U. *J. Alloys Compd.* **1997**, *246*, 193−208. Lachwa, H.; Reinen, D. *Inorg. Chem.* **1989**, *28*, 1044−1053.
(6) Goodenough, J. B.; Ruiz-diaz, J. E.; Zhen, Y. S. *Solid State Ionics* **1990**, *44*, 21.
(7) Parsons, T. G.; D'Hondt, H. D.; Hadermann, J.; Hayward, M. A. *Chem. Mater.* **2009**, *21*, 5527−5538.
(8) Berastegui, P.; Hull, S.; García-García, F. J.; Eriksson, S.-G. *J. Solid State Chem.* **2002**, *164*, 119−130.
(9) Speakman, S. A.; Richardson, J. W.; Mitchell, B. J.; Misture, S. T. *Solid State Ionics* **2002**, *149*, 247−259.
(10) Speakman, S. A.; Misture, S. T. *Mater. Sci. Forum* **2001**, *378−381*, 336−339.
(11) Kobayashi, T.; Hasesaka, A.; Hibino, M.; Yao, T. *Trans. Mater. Res. Soc. Jpn.* **2008**, *33*, 1077−1080.
(12) Laha, S.; Sharma, R.; Bhat, S. V.; Reddy, M. L. P.; Gopalakrishnan, J.; Natarajan, S. *Bull. Mater. Sci.* **2011**, *34*, 1257−1262.
(13) Larson, A. C.; Von Dreele, R. B. *General Structure Analysis System (GSAS)*; Los Alamos National Laboratory Report LAUR; 2004; pp 86−784.
(14) *EXPGUI*, a graphical user interface for *GSAS*: Toby, B. H. *J. Appl. Crystallogr.* **2001**, *34*, 210.
(15) Bain, G. A.; Berry, J. F. *J. Chem. Educ.* **2008**, *85*, 532−536.
(16) Sherif, M. E.; Bayoumi, O. A.; Sokkar, T. Z. N. *Color Res. Appl.* **1997**, *22*, 32.
(17) Hassan, A. K.; Pardi, L. A.; Krzystek, J.; Sienkiewicz, A.; Goy, P.; Rohrer, M.; Brunel, L.-C. *J. Magn. Reson.* **2000**, *142*, 300.
(18) Fischera, W.; Reckb, G.; Schoberc, T. *Solid State Ionics* **1999**, *116*, 211−215.
(19) Pardi, L. A.; Krzystek, J.; Telser, J.; Brunel, L. C. *J. Magn. Reson.* **2000**, *146*, 375−378.

(20) Alario-Franco, M. A.; Gonzalez-Calbet, J. M.; Grenier, J. C. *J. Solid State Chem.* **1983**, *49*, 219−231.

(21) D'Hondt, H. D.; Abakumov, A. M.; Haderman, J.; Kalyuzhnaya, A. S.; Rozova, M. G.; Antipov, E. V.; Van Tendeloo, G. *Chem. Mater.* **2008**, *20*, 7188−7194.